Mitigating distortions during debinding of a monolithic solid oxide fuel cell stack using a multiscale, multiphysics model

Miao, Xing-Yuan; Pirou, Stéven; Frandsen, Henrik Lund

Published in:
Journal of the European Ceramic Society

Link to article, DOI:
10.1016/j.jeurceramsoc.2022.12.059

Publication date:
2023

Document Version
Publisher's PDF, also known as Version of record

Journal of the European Ceramic Society 43 (2023) 1992–2001

Contents lists available at ScienceDirect

Journal of the European Ceramic Society

journal homepage: www.elsevier.com/locate/jeurceramsoc

Original article

Mitigating distortions during debinding of a monolithic solid oxide fuel cell stack using a multiscale, multiphysics model

Xing-Yuan Miao *, Stéven Pirou, Henrik Lund Frandsen

Department of Energy Conversion and Storage, Technical University of Denmark, Building 310, Fysikvej, DK 2800, Lyngby, Denmark

ARTICLE INFO

Keywords:
Solid oxide fuel cell stack
Monolith
Debinding
Pore-former
Computational modelling
Multiscale
Multiphysics

ABSTRACT

Improving the power density of solid oxide fuel cell stacks would significantly enhance this technology for transportation. Using a monolithic structure to downsize the stack dimension offers a key to elevate the power density of solid oxide fuel cell stacks. This innovative design is promising but manufacturing is a challenge. The monolith is co-sintered in one firing step, and the gas channels are formed by burning off sacrificial organic materials. Structure distortion or fracture was observed in post-mortem investigations. In this work a multiscale, multiphysics modelling approach is proposed to describe and resolve this challenge in the debinding process occurring in a monolithic stack, i.e. the burning of organics and transportation of gases through the gradually opening microstructure, as well as the pressure build-up in the microstructure due to gas development. Simulation results show that a prominent pressure peak is experienced in the stack when a plasticiser (polyethylene glycol) and a pore-former (polymethyl methacrylate) are decomposed simultaneously. To reduce the high pressures, we investigate two possible strategies: (i) changing the mixture of organic additives; (ii) modifying the debinding temperature profile. Three tapes with different pore-formers are prepared, and the generated pressures during debinding of the three stacks are compared. The corresponding stack shapes after debinding are recorded. Numerical investigations show a good agreement with the post-mortem observations. By changing the composition of organics the distortion or fracturing of the stack can be avoided. Furthermore, to facilitate stack manufacturing, the high pressures can also be reduced by adjusting the heating rates and dwell temperatures of debinding. By using the new temperature profile suggested by the simulation study, the duration of debinding can also be reduced.

1. Introduction

Solid oxide fuel cell (SOFC) stacks are receiving attention due to the increasing demands of energy efficiency for future transportation. For transportation SOFCs are required to have small dimensions yet high power density, guaranteed structural stability and moderate durability (e.g. lifetime ~4,000 h) [1–4]. In particular structural stability is needed to allow for the dynamic operations associated with the fast thermal cycling in mobile applications.

Using metal materials as mechanical supports for the cell, combined with monolithic design endows high power density, superior mechanical performance, and economic competitiveness to the SOFCs [5–7]. A monolithic design integrates cell support, gas channels, and interconnects into a single layer, unlike conventional stacks, thereby significantly reducing the stack height and increasing the power density [8]. Manufacturing monolithic SOFCs is however a challenge. For example, the thermal removal of organics adopted to form the gas channels will produce large amounts of gases in the stack, which can lead to significant distortion or fracturing of the structure.

Thermal debinding is one of the most critical processes for manufacturing electrochemical cells through sintering e.g. solid oxide electrolysis cells (SOECs) and SOFCs from green tapes prepared by tape-casting and laminating. This is especially true for the manufacture of monolithic stacks with gas channels [9–12]. The porosity of a sintered body will increase during the thermal decomposition of organic additives, along with the generation of large amounts of gases, which will produce high transient pore pressures within the structure. The high pressure may damage the green tape, causing distortions or fractures, as shown in Fig. 1, [9,13,14].

Previous studies of thermal debinding reported in the literature have confirmed the potential distortion or damage of the structure, as elaborated in the following. Cracks formed during thermal debinding of a wax-based zirconia–binder system was reported in [15]. Distortion of complex-shaped Ti-6Al-4V parts after thermal debinding of a multi-component binder system with high molecular binder content

* Corresponding author.
E-mail address: ximi@dtu.dk (X.-Y. Miao).

https://doi.org/10.1016/j.jeurceramsoc.2022.12.059
Received 18 July 2022; Received in revised form 20 December 2022; Accepted 23 December 2022
Available online 28 December 2022

Nomenclature

Throughout the article bold face symbols denote tensors and vectors. Normal face letters represent scalar quantities.

Greek symbols

$\boldsymbol{\kappa}$	Permeability tensor [m^2]
$\boldsymbol{\lambda}$	Thermal conductivity tensor [$W\ K^{-1}\ m^{-1}$]
μ	Dynamic viscosity [Pa s]
ϱ	Density [$kg\ m^{-3}$]
τ	Tortuosity [–]
ϕ	Porosity [–]

Roman symbols

A	Pre-exponential factor [s^{-1}]
c	Molar concentration [$mol\ m^{-3}$]
C_0	Kozeny's constant [–]
c_p	Specific heat capacity [$J\ K^{-1}\ kg^{-1}$]
D	Diffusion coefficient [$m^2\ s^{-1}$]
D_S	Fractal dimension scale of pore-solid interface [–]
d_w	Effective grain size [m]
E	Activation energy [$J\ mol^{-1}$]
k	Reaction rate [$kg\ m^{-3}\ s^{-1}$]
M	Molar mass [$kg\ mol^{-1}$]
m_i	Mass of organic additive i [–]
r_h	Mean hydraulic radius [m]
R_s	Specific gas constant [$J\ K^{-1}\ kg^{-1}$]
R_α	Effective thermal resistance of layer α in a single repeating unit, α = IC, MS, CH, AL, EL, CL [$K\ m\ W^{-1}$]
T	Temperature [K]
v	Volume fraction [–]
w	Mass fraction [–]

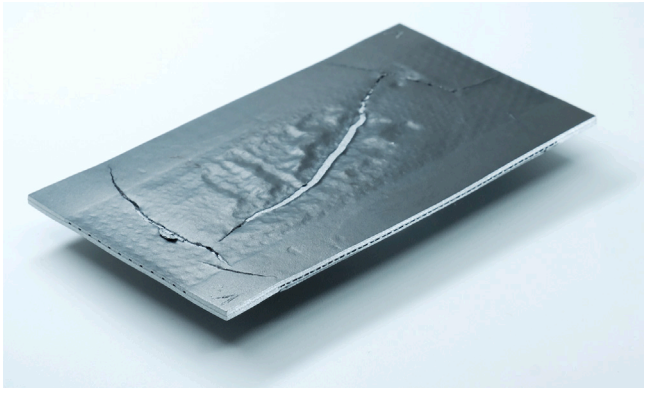

Fig. 1. Picture of a SOFC distorted and fractured after the debinding process, cf. [8].

was evaluated by [16]. Distortion of the structure after thermal debinding of a high-density polyethylene binder system was observed by [17]. The driving forces that cause the failure are diverse. For example, high stresses, high internal pressures, viscous creep flow can lead to distortion or fracturing of a structure. The diversity of failure mechanisms makes it very difficult and time-consuming to investigate through experiments. Seeking failure mechanisms and potential optimisation strategies using numerical models is considered much more efficient and comprehensive compared to experimental methods. For example, in the thermal debinding of powder injection moulding compact, distortion due to the non-uniform distribution and flow of the polymer was examined through a numerical simulation [18]. A three-dimensional model of thermal debinding was presented to determine the binder distribution, temperature distribution, and deformation in metallic components during the thermal debinding process [19]. The migration mechanisms of fluids within the green body were also determined using numerical models. In the early stage of thermal debinding of green bodies with organics (referred to as first debinding step), the transport of liquids is mainly driven by capillary forces as stated in [20,21]. In the stage of thermal debinding prior to sintering when many pores have been formed (second debinding step), pressures become the dominating driving force for the failures [18,21,22]. The transport of gases depends on the flow resistance and pressure gradients [23].

The multi-component and multiphysics nature of solid oxide cell (SOC) stacks impose computational challenges in the simulation of stack performance. Too many geometric details and heterogeneities would lead to a high computational demand in numerical modelling of multiphysics processes. Running a transient three-dimensional multiphysics stack model is even more computationally expensive. In [24], it took 44 h to obtain four-seconds transient-dynamic states of a repeating unit of an SOFC stack. Conducting complex parametric studies to determine critical parameters results in even higher computational costs. However, in cell manufacturing, we expect a fast modelling examination on e.g. decomposition of organics, cause of distortions or cracks to guide experimental design, saving time and expense. This would benefit the manufacturers. Homogenisation treatment is useful when modelling structures with repeating complex geometries. Navasa et al. [25] developed a new homogenised stack model to simulate all relevant physical phenomena with very low computational cost. Miao et al. [26] further developed a novel multiscale multiphysics modelling framework using homogenisation and localisation to examine local mechanical failures in full SOC stacks. The microstructural characteristics of cell components may have a significant impact on the macroscopic response of an SOC stack. For example, the microstructural morphology e.g. pore structures affect the macroscopic properties e.g. permeability, mechanical stiffness. Zhuang et al. [27] developed a multiscale homogenised model of porous material, linking the evolving microstructure to the macroscopic mechanical response.

To address the computational challenge, in this work we present a computational-efficient three-dimensional multiscale multiphysics modelling framework, focusing on the main physical phenomena occurring during the debinding process, i.e. fluid flow in porous media, heat and mass transfer, as well as chemical reactions. This model is realised with the commercial software COMSOL Multiphysics 5.6. The objective of this work is two-fold: (i) to quantify the transient pressure build-up during the debinding of SOFC monoliths, and (ii) to investigate potential optimisation methods to reduce the critical pressures that might damage a stack.

The present article is organised as follows. In Section 2, the production of monolithic SOFC stacks is briefly introduced. The overall model concept is described in Section 3. The relevant experiments are described in Section 4. In Section 5, material and structural properties used in debinding modelling are determined. Particular attention is placed on the identification of kinetic parameters associated with the reaction kinetics model and effective material properties for the stack modelling. A comprehensive analysis of debinding monolithic SOFC stacks including optimisation efforts towards reducing the risk of stack damages is conducted in Sections 6 and 7. The main conclusions of this paper are stated in Section 8.

2. Production of a monolithic solid oxide fuel cell stack

A single repeating unit (SRU) contains seven layers: an anode layer, an electrolyte layer, a cathode layer, two metal support layers containing gas flow channels, and two interconnect layers, as shown in

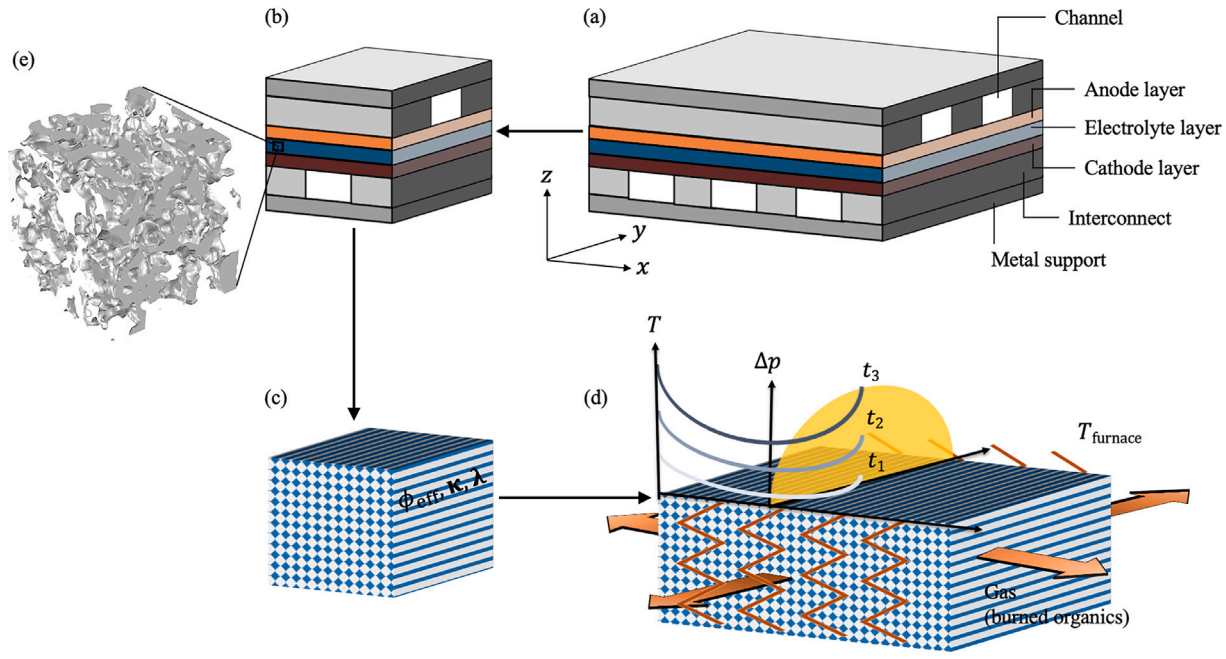

Fig. 2. Schematic of multiscale modelling for thermal debinding of SOFC monoliths. (a) An SRU monolith. (b) One-channel repeating unit with a highlight of microstructural details. (c) Equivalent porous medium with effective material properties. (d) Modelling debinding process. (e) 3D reconstruction of porous microstructure [28,29].

Fig. 2(a). The interconnect and metal support are made of steel (dense Fe22Cr, provided by Sandvik Osprey Ltd, UK). The electrolyte is made of scandia-doped yttria-stabilised zirconia (ScYSZ, provided by Daiichi Kigenso Kagaku Kogyo Co., Ltd., Japan). The anode and the cathode are composed of ScYSZ-Fe22Cr composite. The gas channels are placed between the interconnects and the electrodes, and they are formed from the thermal removal of tapes made of pore-formers.

The slurries prepared for the monolith contains three types of organic additives: binder (polyethylene glycol B60H, provided by Kuraray), plasticisers (polyethylene glycol S2075, provided by Solutia; polyethylene glycol PEG, provided by Sigma – Aldrich Products – Life Science), and pore-formers (graphite, provided by AMG Graphite – Graphit Kropfmühl GmbH; polymethyl methacrylate PMMA, provided by Esprix Technologies). Three pore-former tapes made of 100 % PMMA, 50/50 vol % mixture of graphite and PMMA, and 100 % graphite were prepared. The pore-former powders were ball-milled in a solvent for 72 h using polyethylene bottles and zirconia balls. A mixture of butan-2-one and ethanol in a 2 : 1 weight ratio was used as solvent for the gas channel slurry. The amount of solvent corresponds to 34.52 wt % of slurry. Afterwards, the mixture of binder and plasticisers were added and the slurries were homogenised for an additional 24 h by ball milling. The viscosity of the suspensions were analysed and adjusted either by adding or removing solvent. Prior casting, the slurries were filtered and de-aired.

The dimensions of the SRU components are listed in Table 1. The basic material properties of the components are provided in Table 2, and the details of the slurry compositions in each layer are given in Table 3.

In monolithic design, the cell support, gas channels, and interconnects are integrated into a single support layer. The cell with electrolyte sandwiched between the air electrode and the fuel electrode is placed between the support layers. Seals along the cell sides and the support layers are also integrated.

Tape casting, lamination, co-sintering, and catalyst infiltration are used for manufacturing the monolith. Particularly, the monolith is co-sintered in one firing step, and the gas channels are formed by burning off sacrificial organic materials. A detailed description of the concept and manufacturing of monolithic SOFC stacks can be found in [8].

Table 1
Dimensions of the SRU.

Material layers	Length L / mm	Width W / mm	Height H / mm
Interconnect (IC)	90	52	0.07
Anode (AL)	90	52	0.02
Electrolyte (EL)	90	52	0.02
Cathode (CL)	90	52	0.02
Metal support (MS)	0.2	52	0.20
Gas channel (CH)	0.8	52	0.20

Table 2
Material properties of stack components.

Materials	Density ρ / kg m^{-3}	Thermal conductivity λ / W K^{-1} m^{-1}	Molar mass M / g mol^{-1}	References
ScYSZ	6100	2.00	–	[30]
Fe22Cr	7400	16.0	–	[31]
PEG	1000	0.19	370	[32]
PMMA	1180	0.25	100	[33]
B60H	1070	0.24	142	[34]
S2075	1130	0.19	402	[32]
Graphite	2250	134	12.0	[35]

3. Modelling concept

The debinding model is realised using a multiscale modelling approach. The modelling schematic is illustrated in Fig. 2. So-called homogenisation [25,26] is applied to the stack to build the macroscale model with the following physical phenomena: fluid flow in porous media, heat and mass transport, and chemical reactions. The relevant physical processes are described using flow equation for porous media, heat conduction equation, and convection–diffusion equation, respectively, see Table 4. The constituents of all layers are averaged over the stack, forming an equivalent porous medium at the macro scale as shown in Fig. 2(c). This equivalent porous material is assumed to be homogeneous. The organics are thus distributed over the entire stack volume. The decomposition of organics will occur everywhere in the stack, and the generated gases during debinding will migrate through the whole volume. Thus the mass balances in the transient simulations refer to the average masses.

Table 3
Mass of components in each layer.

Materials	IC	AL	EL	CL	MS	CH (mass for 2 layers)	Mass in a repeating unit / g
ScYSZ	0.000	0.065	0.810	0.065	0.000	0.000	0.943
Fe22Cr	1.694	0.118	0.000	0.118	2.450	0.000	8.524
PEG	0.070	0.011	0.046	0.011	0.125	0.069	0.596
PMMA	0.000	0.009	0.000	0.009	0.000	0.352	0.721
B60H	0.124	0.020	0.081	0.020	0.220	0.122	1.052
S2075	0.066	0.010	0.043	0.010	0.117	0.064	0.558
Graphite	0.134	0.016	0.000	0.016	0.340	0.000	0.980

Note: The polymerisation degree of the PEG used in the slurry is 9.

Table 4
Mathematical models applied in the debinding model.

Physical quantities	Mathematical models	Coupling terms
Pressure	$\frac{1}{R_s T}\frac{\partial(\phi p)}{\partial t} - \rho \mathrm{div}\left(\frac{\boldsymbol{\kappa}}{\mu}\mathrm{grad}p\right) - k = 0$ (1)	T, c
Temperature	$(\rho c_p)_{\mathrm{eff}}\frac{\partial T}{\partial t} + \rho c_p \mathrm{grad}T \cdot \mathbf{u} - \mathrm{div}\left(\boldsymbol{\lambda}\mathrm{grad}T\right) = 0$ (2)	**u** (Darcy velocity), c
Molar concentration	$\frac{\partial(\phi c)}{\partial t} + \mathrm{div}\left(\mathbf{u}c - \phi D \mathrm{grad}c\right) - \frac{k}{M} = 0$ (3)	**u** (Darcy velocity), T

Note: The definitions of all relevant parameters are given in Nomenclature.

Effective material parameters are used in the macroscale modelling to properly describe the mass transport as if all the geometric details were included. Some equivalent material properties can be determined using the volume-weighted method, e.g. porosity. For some material properties that are strongly affected by the microstructural characteristics of the stack components, e.g. permeability, a detailed microscale model is built from a three-dimensional reconstructed geometry to reflect the microscale porous structure in the macroscale stack model, e.g. determining the relation between the permeability and porosity of the equivalent porous material. The microstructural data from the studies by [28,29] are used for the purpose, see Fig. 2(e).

4. Experimental

4.1. Thermogravimetric analysis

Thermogravimetric analysis (TGA) was performed to investigate at which temperatures the organic additives would be removed and obtain reaction kinetics parameters. A thermogravimetric (TG) analyser (STA 409 CD – Simultaneous TG-DSC) manufactured by NETZSCH – Gerätebau GmbH, Germany was used to measure mass changes of organics. Green tapes were placed in alumina crucibles and heated following the heating profile shown in Fig. 3 with a heating rate of 0.25 °C min^{-1}. To ensure a complete decomposition of organic additives, the temperature is held for 4 h at 200 °C and 410 °C, and 6 h at 600 °C, respectively. Pictures of the TG analyser and the samples (i.e. rolled green tapes) are shown in Supplementary Figure S1(a) and S1(b), respectively.

4.2. Thermal debinding of SOFC monolith

The monolithic SOFC stack presented in the green state in Fig. 4 is thermally treated in a chamber furnace (LH 15/12 – LF 120/14, Nabertherm GmbH, Germany) from room temperature to 600 °C in air to remove the organic additives contained in the tapes. To smoothly burn off the organics, heating ramps of 0.25 °C min^{-1} and dwell times of 4 h, 4 h, and 6 h are used at 200 °C , 410 °C , and 600 °C respectively.

5. Determination of material parameters

In this section, material parameters that will be used to model the debinding process of monolithic SOFCs are determined by experimental and numerical approaches.

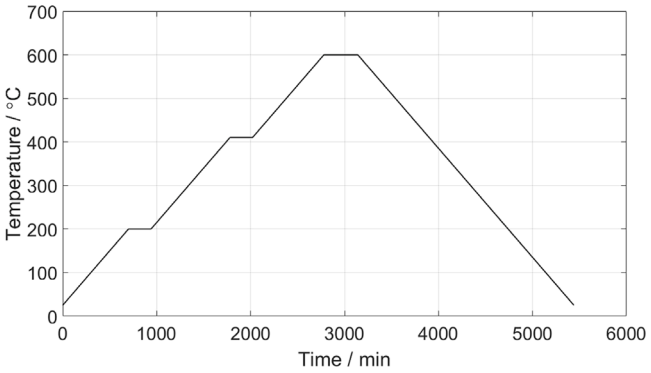

Fig. 3. Heating profile of TGA.

Table 5
Chemical equations of thermal decomposition of the organic additives.

Materials	Chemical equations
PEG	$C_{16}H_{34}O_9 + 20\ O2 \rightarrow 16\ CO_2 + 17\ H_2O$
PMMA	$C_5H_8O_2 + 6\ O_2 \rightarrow 5\ CO_2 + 4\ H_2O$
B60H	$C_8H_{14}O_2 + \frac{21}{2}\ O2 \rightarrow 8\ CO_2 + 7\ H_2O$
S2075	$C_{22}H_{42}O_6 + \frac{59}{2}\ O2 \rightarrow 22\ CO_2 + 21\ H_2O$
Graphite	$C + O_2 \rightarrow CO_2$

5.1. Chemical equations of organics degradation

The chemical equations for the thermal decomposition of organic additives in pore-former green tapes are detailed in Table 5. Note that the intermediate stages of thermal decomposition of the organic additives are neglected in the models. CO_2 and H_2O are considered the final products.

5.2. Reaction kinetics parameters

The activation energy and pre-exponential factor of each organic component are determined by fitting the reaction kinetics models to the results from the TG experiment, see Table 6. The kinetic model is written below, which describes the change of mass $\dot{m}$ as a function of temperature T and the current mass m [36].

$$\dot{m}_i = \frac{\mathrm{d}m_i}{\mathrm{d}t} = -A_i e^{\frac{-E_i}{RT}} m_i \quad (4)$$

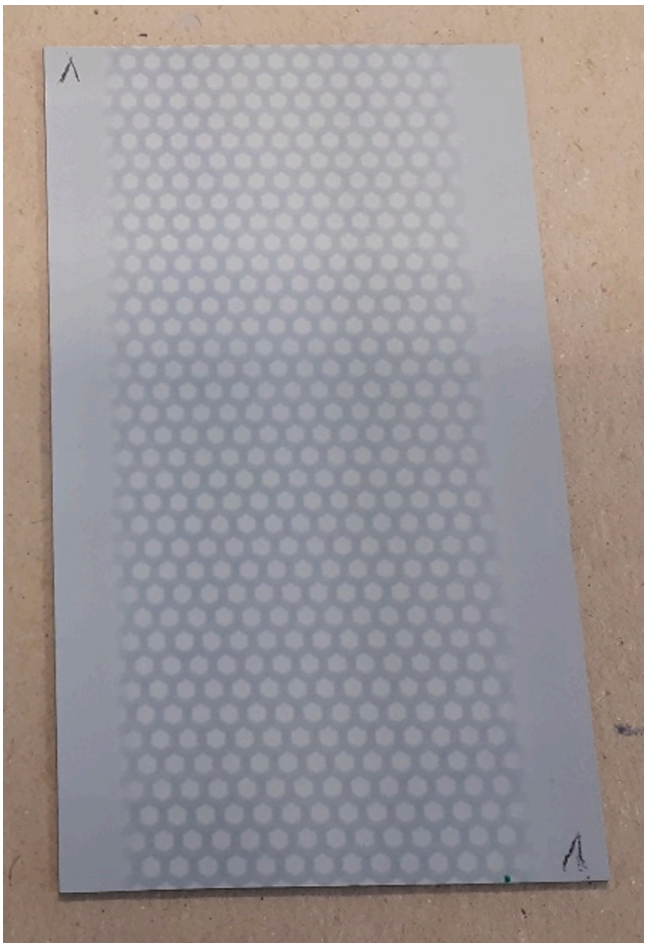

Fig. 4. Picture of a monolithic SOFC stack in green state (stack dimension: 90 mm × 52 mm). The gas channels are formed using honeycomb shaped pore-former tapes [8].

Table 6
Activation energies and pre-exponential factors of organic additives.

Materials	Activation energy E / J mol^{-1}	Pre-exponential factor A / min^{-1}
PEG	8.22×10^4	2.57×10^7
PMMA	8.87×10^4	1.27×10^7
B60H	9.09×10^4	1.94×10^6
S2075	9.41×10^4	3.09×10^5
Graphite	1.05×10^5	1.06×10^4

where i is organic component identifier in subscript, m represents the mass of organics. The total change of mass per time is

$$\dot{m}_{\text{total}} = \sum_{i=1}^{5} \dot{m}_i w_i \tag{5}$$

Note that the current models do not describe the many decompositions steps which are needed to describe the very fast ramp rates. Due to the low heating ramp rates used in this work, the activation energies and pre-exponential factors are assumed to be constants [37].

Fig. 5 shows the mass variations of organic additives as a function of the temperature. The sequence of thermal removal is PEG, PMMA, B60H, S2075, and graphite, as shown in Fig. 5(a). Fig. 5(b) shows the mass–temperature curves obtained from the kinetic model with the fitted reaction kinetics parameters shown in Table 6 and the TG experiment. The agreement between the two approaches suggests that the applied kinetic models are suitable for describing the reaction kinetics of the organic additives.

5.3. Thermal conductivity

The equivalent anisotropic thermal conductivity tensor is written as

$$\boldsymbol{\lambda} = \begin{bmatrix} \lambda_x & 0 & 0 \\ 0 & \lambda_y & 0 \\ 0 & 0 & \lambda_z \end{bmatrix} \tag{6}$$

where the three components are determined in terms of Fig. 6.

$$\lambda_x = \lambda_y = \frac{2}{R_{\text{IC}}} + \frac{1}{2R_{\text{MS}} + R_{\text{CH}}} + \frac{1}{R_{\text{AL}}} + \frac{1}{R_{\text{EL}}} + \frac{1}{R_{\text{CL}}} + \frac{2}{R_{\text{MS}}} + \frac{1}{R_{\text{CH}}} \tag{7}$$

$$\lambda_z = \frac{2R_{\text{MS}} + R_{\text{CH}}}{\left(2R_{\text{IC}} + R_{\text{AL}} + R_{\text{EL}} + R_{\text{CL}}\right)\left(2R_{\text{MS}} + R_{\text{CH}}\right) + R_{\text{MS}} R_{\text{CH}}} \tag{8}$$

where R_α represents the effective thermal resistance of layer α. Note that $R_\alpha(c_{\text{organics}})$ will change with the temperature due to the decomposition of organic components, and so the other physical properties of the stack, i.e. ρ_{avg}, ϕ, $\boldsymbol{\kappa}$.

5.4. Permeability

The permeability as a function of the changing porosity of the porous media is determined based on the Kozeny–Carman equation [38–40], which provides good results for similar microstructures [29].

$$\kappa = C_0 \tau^2 \frac{\phi^3}{(1-\phi)^2} d_w^2 \tag{9}$$

with the tortuosity

$$\tau = \phi^{\frac{2-2D_{\text{S}}}{2-D_{\text{S}}}} \tag{10}$$

where κ represents the permeability, τ the tortuosity, and ϕ the porosity. C_0 is the Kozeny's constant, D_{S} the fractal dimension scale of pore-solid interface, and d_w the effective grain size.

To implement Eq. (9) into the stack model, the product of C_0 and d_w^2 needs to be obtained first. This product can be determined with an extracted microstructure sample. By reconstructing this sample from X-ray computed tomography, its microscale geometry can be implemented into finite element software to evaluate the current permeability κ and porosity ϕ [28]. D_{S} is also estimated to accommodate the specific characteristics of the stack model. With the known κ, ϕ, and D_{S}, $C_0 d_w^2$ can then be obtained by combining Eq. (9) and Eq. (10). In this work, we assume that $C_0 d_w^2$ will not change during the debinding process.

5.5. Porosity

The porosity in debinding process is determined in terms of the average volume fraction of each component, i.e. $\phi = 1 - \upsilon_{\text{Fe22Cr}} - \upsilon_{\text{ScYSZ}} - \upsilon_{\text{PEG}} - \upsilon_{\text{PMMA}} - \upsilon_{\text{B60H}} - \upsilon_{\text{S2075}} - \upsilon_{\text{Graphite}}$. The average volume fraction of each component is determined by dividing the volume of the component by the total volume of the stack. With the burning of organics in the debinding process, the volume fractions of PEG, PMMA, B60H, S2075 and graphite will decrease correspondingly, and the porosity will dramatically increase due to the removal of organic additives. To simulate that the gasses can diffuse through the partially liquid binder at the point of decomposition, we ascribe an initial porosity of 0.1.

6. Simulations of debinding monolithic SOFCs

6.1. Base case

A monolithic SOFC made of PMMA pore-former tape is modelled as a base case. The mass of each component in each layer is given in Table 3. The same debinding temperature profile used in the debinding experiments (Fig. 3, Section 4) is applied in this base case model.

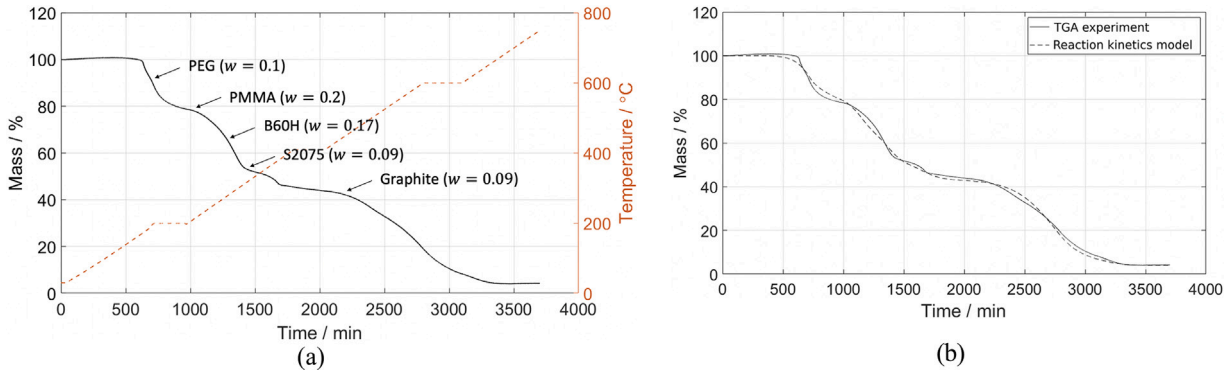

Fig. 5. Mass change of the pore-former tape over temperature. (a) TG measurement with heating rate of 0.25 °C min^{-1}; (b) reaction kinetics modelling vs. TG measurement.

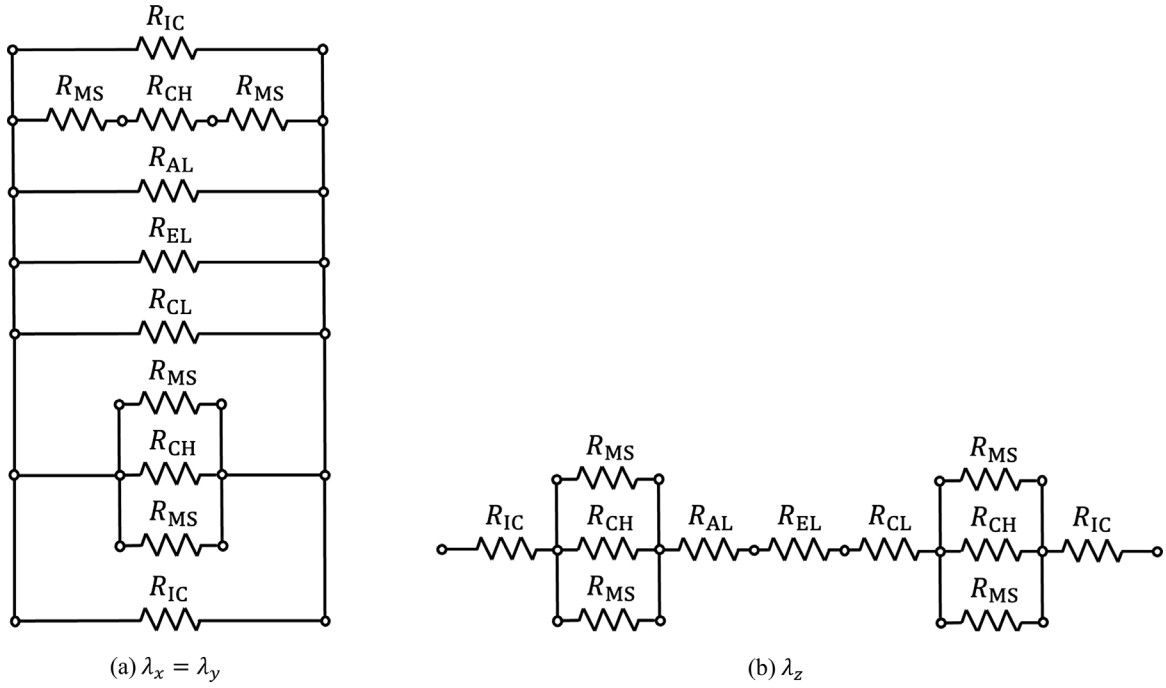

Fig. 6. Calculation of effective thermal conductivities of the stack. (a) The equivalent thermal conductivity corresponding to the x and y direction shown in Fig. 2(a) and (b) the equivalent thermal conductivity in z direction.

Table 7
Initial conditions used for the simulations.

Variables	Values	Units	Description
c_{PEG}	328	mol m^{-3}	Initial concentration of PEG
c_{PMMA}	1467	mol m^{-3}	Initial concentration of PMMA
c_{B60H}	1467	mol m^{-3}	Initial concentration of B60H
c_{S2075}	282	mol m^{-3}	Initial concentration of S2075
$c_{Graphite}$	16 619	mol m^{-3}	Initial concentration of graphite
p_{ref}	1	atm	Reference pressure
T_{ini}	20	°C	Initial temperature

6.2. Initial and boundary conditions

The initial conditions used for the simulations are presented in Table 7. The initial temperature is set to the room temperature, i.e. 20 °C. The temperature as a function of time $T(t)$ is applied on all boundaries of the stack volume representing the heating profile for debinding. The reference pressure is 1 atm. The generated gases can flow out from all boundaries.

6.3. Numerical settings and computational times

The debinding model is realised with the commercial software COMSOL Multiphysics 5.6. A discretisation of 1110 hexahedral elements with a uniform element size of 3 mm is applied. A direct solver is used for resolving the linear system. Newton iterations are performed to solve non-linearities with a relative tolerance of 10^{-4}. All calculations are performed on a workstation with an Intel(R) Xeon(R) W-2135 CPU @ 3.70 GHz 6 Cores, and 128 GB RAM. Simulating a thermal debinding process of 3140 min (~52 h) takes 50 min.

6.4. Simulation of base case

Fig. 7 shows the molarity changes of organic additives over the debinding cycle. The decomposition behaviour of organic additives is consistent with the results of the TG measurement shown in Fig. 5(a). The generation and migration of gases during the thermal removal of the organics result in the change of porosity and pressure are shown in Fig. 8 and Fig. 9. Five peak pressures (14, 4, 3, 0.6, and 0.4 mbar) are found at 190 °C, 240 °C, 283 °C, 366 °C, and 573 °C, respectively. The pressure peaks occur when large amounts of gases are generated

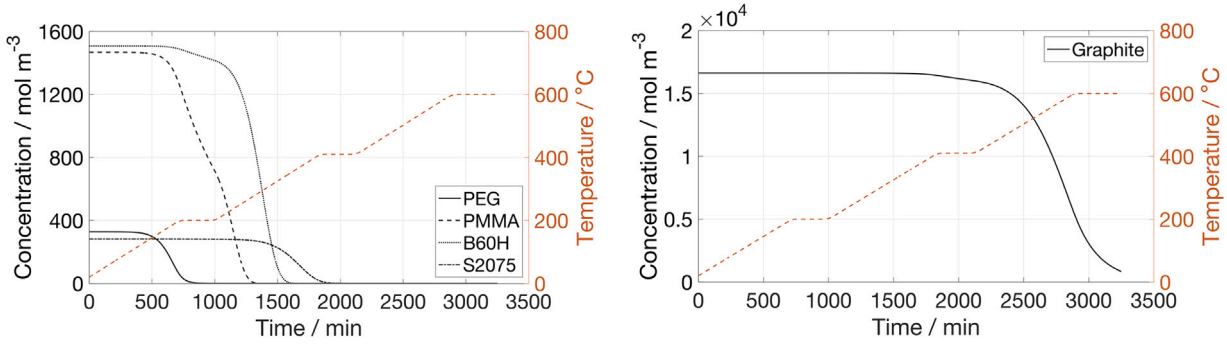

(a) Molarity change of PEG, PMMA, B60H, and S2075

(b) Molarity change of graphite

Fig. 7. Change of molarity per unit volume of organic additives.

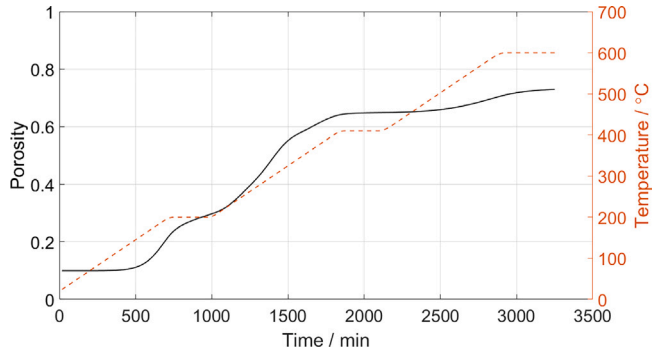

Fig. 8. Porosity change over the time.

within a short period. Pressure variations inside the stack volume are represented by the pressure variations along the centre lines in the width and height direction at the pressure peaks in the insert images of Fig. 9. Note that as the heat transport in the stack is significantly faster than the heating ramp of the furnace, the temperature inside the stack is uniform.

7. Process optimisation

As can be seen in Fig. 9, the highest pressure peak corresponds to the thermal removal of PEG and PMMA. The decomposition of PEG and PMMA occurs at similar temperatures (160 °C ~ 180 °C, cf. Fig. 7(a)), which contributes to generating large amounts of gases in a short period, leading to deformation and eventually to fracturing of the stack, as shown in Fig. 1. To better distribute the amount of developed gases over the temperature and time, two strategies are possible: (i) change the mixture of organic additives; (ii) modify the debinding temperature profile.

7.1. Modification of pore-former composition

The amount of PEG can be reduced by modifying the mixture of plasticiser or reducing the PMMA content in the mixture of pore-formers. Particularly, the type of pore-former has a significant impact on the pressure build-up, as the relative volume percentage of pore-former in the stack is much higher than that of other components.

To confirm whether the damage of the stack results from the peak pressures, we compare three SOFC stacks containing three different pore-former tapes: 100 % PMMA, 50/50 vol % mixture of graphite and PMMA, and 100 % graphite, respectively. The pressures generated during the debinding of the three monoliths are calculated using the proposed stack model, and the corresponding stack shapes after debinding are recorded with the debinding experiments.

As can be seen in Fig. 10, the highest pressure peak in the monolith made of PMMA pore-former tape (maximum: 14 mbar) is much higher than that in the other two stacks. The highest pressure in the monolith made of graphite/PMMA mixture and made of graphite pore-former tape are 9 mbar and 7 mbar, respectively. Using graphite to partly/fully replace the PMMA pore-former can significantly reduce the pressure build-up in the early stage of the debinding process. This is because (i) the total mass of PMMA is reduced, resulting in a significant reduction of the molar volume of gases, and (ii) the graphite decomposes after 400 °C, where other organics have been almost completely decomposed. The simulation results were consistent with the experimental observations. Fig. 10 also shows the post-mortem pictures of the three stacks. It can be seen that the stack composed of PMMA pore-former tape was distorted and damaged, while the other two stacks remained flat and intact, suggesting that reducing the build-up pressures can lower the risk of fracturing the stack during the debinding process.

Fig. 11 shows the scanning electron microscopy (SEM) images of monoliths after debinding. From a representative cross-sectional micrograph of the cell made of PMMA pore-former tape, i.e. Fig. 11(a), we can see that multiple cracks occurred in the monolith when PMMA sacrificial material was used to form the gas channels. The thermal removal of PEG and PMMA in the temperature range 160 °C ~ 200 °C provokes significant damages to the monolith. On the contrary, no cracks occurred in the monolith made of graphite/PMMA mixture, as can be seen in Fig. 11(b).

7.2. Modification of debinding temperature profile

If the stack manufacturer is reluctant to modify the slurry composition, the high pressures generated during the debinding process can also be significantly reduced by adjusting the debinding temperature profile. By using varied heating rates in different debinding periods, the pressures can also be reduced without changing the composition of organic additives. The base case where the stack is made entirely with PMMA pore-former is used in the following.

Figs. 12(a) and 12(b) show the debinding temperature profiles and the corresponding build-up pressures, respectively. Unlike the constant rate of 0.25 °C min^{-1} used in the original temperature profile, a heating rate of 0.20 °C min^{-1} is used up to 212 °C, and 0.60 °C min^{-1} after 212 °C in the modified temperature profile. Moreover, in the modified temperature profile five dwell temperatures (116 °C, 148 °C, 188 °C, 212 °C, and 600 °C) instead of three (200 °C, 410 °C, and 600 °C) in the original temperature profile is used, as shown in Fig. 12(a). The first four dwells are set at relatively low temperatures from 116 °C to 212 °C to facilitate a slow decomposition of PEG and PMMA. Thus the decomposition of PEG and PMMA are controlled, and the pressures are decreased compared to the original case, see Fig. 12(b).

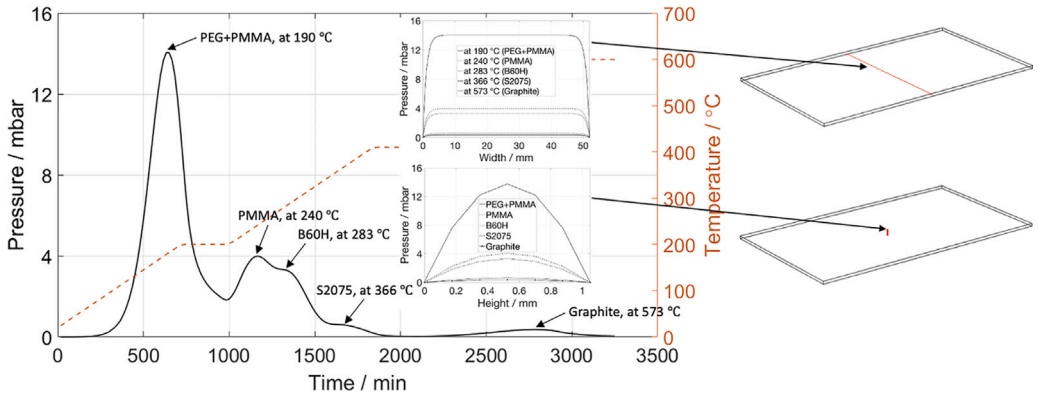

Fig. 9. Pressure build-up over the time at centre location. Inserts show pressure variations along the centre lines in the width and height direction (red lines in the schematic) at the temperatures where pressure peaks occur, i.e. at 190 °C, 240 °C, 283 °C, 366 °C, and 573 °C, respectively, due to the decomposition of specific organic components.

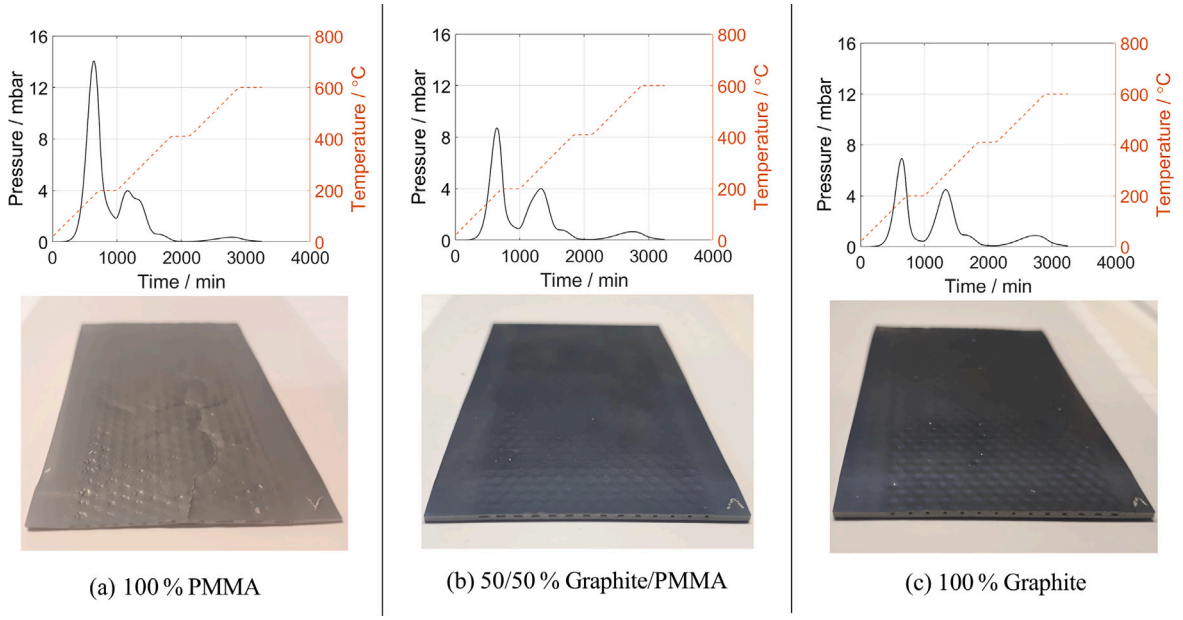

Fig. 10. Pressure build-up in the three SOFC stacks and stack shapes photographed after thermal debinding (stack dimension: 70 mm × 40 mm).

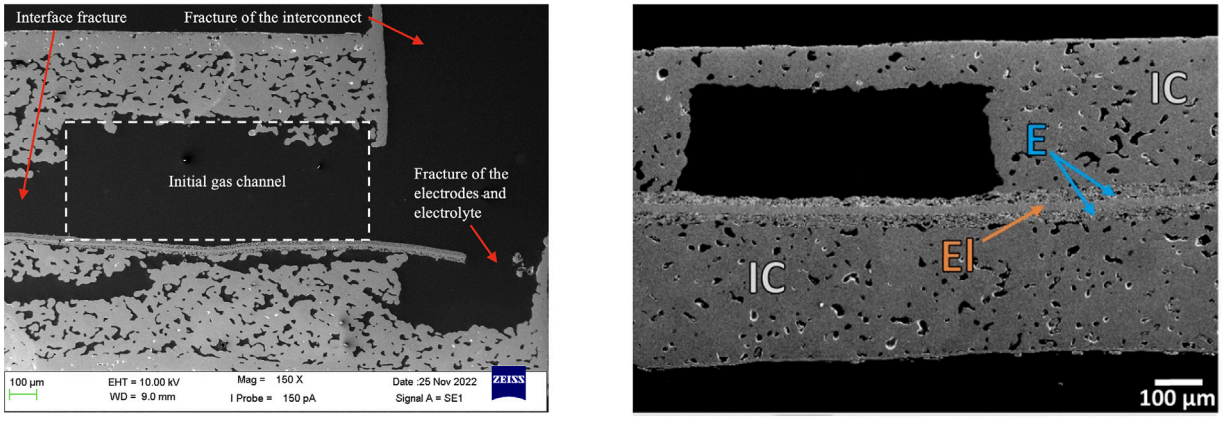

Fig. 11. SEM micrographs of monoliths after debinding. (a) Cross-sectional micrograph of the cell made of PMMA pore-former tape and (b) cross-sectional micrograph of the cell made of graphite/PMMA mixture.

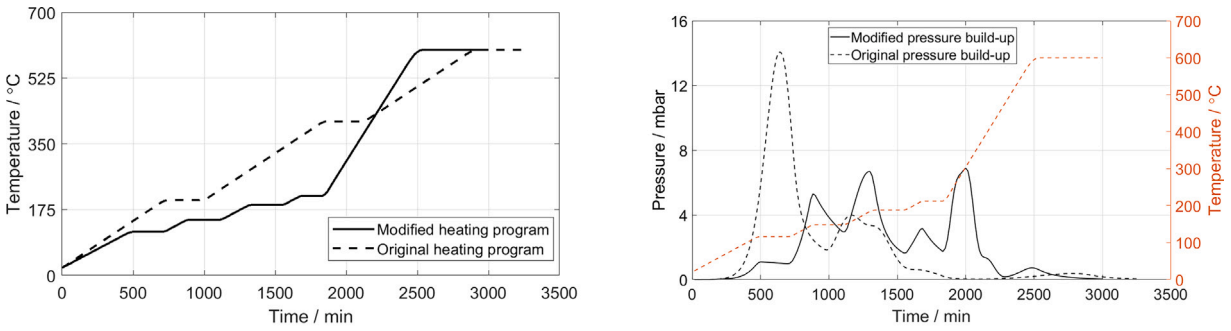

(a) Temperature profile (b) Pressure build-up

Fig. 12. Debinding of the stack made of PMMA pore-former tape using constant (0.25 °C min^{-1}) and varied heating rate (0.2 °C min^{-1} before 212 °C, and 0.6 °C min^{-1} after 212 °C). (a) Comparison of the debinding temperature profiles; (b) comparison of the pressure build-ups.

Note that the pressure build-up per unit volume during decomposition of the graphite is much smaller than that generated during the burning of PEG and PMMA. Thus a high heating rate (0.60 °C min^{-1}) can be adopted in the later stage. Nevertheless, compared to the original temperature profile, a longer temperature dwell (7 h) at 600 °C is applied in the modified debinding procedure for the complete decomposition of the graphite used in the pore-former tape. As can be seen in Fig. 12(b), there are seven pressure peaks generated in the modified debinding procedure. Simulation results show that the highest pressure peak (14 mbar) in the original case is broken into several lower pressure peaks (< 7 mbar), with a 51 % reduction of the highest one. All adjustments made on the debinding temperature profile for the reduction of the pressures also lead to a reduction of the total time for the debinding procedure. Thanks to the relatively fast heating ramp used after 212 °C (0.60 °C min^{-1}), the total time is reduced from 3,140 min to 2,917 min, corresponding to a reduction of 7 % (∼ 4 h) compared to the original debinding cycle.

8. Conclusions

In this work, the driving force that leads to the damage of monolithic solid oxide fuel cell stacks during the debinding process is investigated. The structural responses of stacks composed of different pore-former tapes are determined using a numerical model. A computational-efficient multiscale multiphysics model is proposed to quantify the pressures induced by the thermal decomposition of organic additives. The microstructural properties are determined using a microscale model and are linked to the macroscopic responses of the stacks to the thermal treatment. To greatly reduce the computing time of transient simulations, a homogenisation method is applied to the macroscale model, i.e. the full-scale stack model.

Numerical investigations show a good agreement with the post-mortem observations. Specifically, simulation results show that the gases generated during the debinding of the stack composed of PMMA pore-former tape result in high build-up pressures and this stack are observed distorted and fractured in the post-mortem pictures. Stacks with gas channels formed by having graphite and graphite/PMMA mixture based sacrificial material present lower build-up pressures and these stacks remain flat and intact in the post-mortem pictures.

Furthermore, the highest transient pressures can also be significantly reduced by regulating the debinding temperature profile, i.e. adjusting the dwell temperatures and using varied heating rates. Particularly, by applying the new temperature profile proposed in this work, the total time of the debinding cycle can be reduced.

The reduction of the debinding time through employing an optimised heating profile would increase the manufacturing efficiency of monolithic solid oxide fuel cell stacks, reducing the cost of fabrication. The multiscale model presented in this work can provide qualitative predictions of experimental results and can be used to optimise important parameters of solid oxide cell stack manufacturing (e.g. slurry composition, debinding temperature profiles).

Declaration of competing interest

The authors declare that they have no known competing financial interests or personal relationships that could have appeared to influence the work reported in this paper.

Acknowledgement

The authors gratefully acknowledge the financial support from Plastic Omnium.

Appendix A. Supplementary data

Supplementary material related to this article can be found online at https://doi.org/10.1016/j.jeurceramsoc.2022.12.059.

References

[1] E.D. Wachsman, C.A. Marlowe, K.T. Lee, Role of solid oxide fuel cells in a balanced energy strategy, Energy Environ. Sci. 5 (2) (2012) 5498–5509.
[2] A. Choudhury, H. Chandra, A. Arora, Application of solid oxide fuel cell technology for power generation—A review, Renew. Sustain. Energy Rev. 20 (2013) 430–442.
[3] J. Rechberger, A. Kaupert, J. Hagerskans, L. Blum, Demonstration of the first European SOFC APU on a heavy duty truck, Transp. Res. Procedia 14 (2016) 3676–3685.
[4] M. Fernandes, S.d.P. Andrade, V. Bistritzki, R. Fonseca, L. Zacarias, H. Gonçalves, A. de Castro, R. Domingues, T. Matencio, SOFC-APU systems for aircraft: A review, Int. J. Hydrogen Energy 43 (33) (2018) 16311–16333.
[5] D. Röhrens, F. Han, M. Haydn, W. Schafbauer, D. Sebold, N.H. Menzler, H.P. Buchkremer, Advances beyond traditional SOFC cell designs, Int. J. Hydrogen Energy 40 (35) (2015) 11538–11542.
[6] A. Hagen, P.V. Hendriksen, Progress of SOFC/SOEC development at DTU energy: From materials to systems, ECS Trans. 78 (1) (2017) 145.
[7] A. Hagen, A.C. Wulff, P. Zielke, X. Sun, B. Talic, I. Ritucci, H.L. Frandsen, S. Jensen, W.-R. Kiebach, P.V. Hendriksen, SOFC stacks for mobile applications with excellent robustness towards thermal stresses, Int. J. Hydrogen Energy 45 (53) (2020) 29201–29211.
[8] S. Pirou, B. Talic, K. Brodersen, A. Hauch, H.L. Frandsen, T.L.y. Skafte, A.s.H. Persson, J.V. Hø gh, H. Henriksen, M. Navasa, X.-Y. Miao, X. Georgolamprou, S.P.V. Foghmoes, P.V. Hendriksen, E.R. Nielsen, J. Nielsen, A.C. Wulff, S.H. Jensen, P. Zielke, A. Hagen, Production of a monolithic fuel cell stack with high power density, Nature Commun. 13 (1) (2022) 1–8.
[9] S. Lee, K. Lee, Y.-h. Jang, J. Bae, Fabrication of solid oxide fuel cells (SOFCs) by solvent-controlled co-tape casting technique, Int. J. Hydrogen Energy 42 (3) (2017) 1648–1660.
[10] Z. Gao, H. Wang, E. Miller, Q. Liu, D. Senn, S. Barnett, Tape casting of high-performance low-temperature solid oxide cells with thin La0. 8Sr0. 2Ga0. 8Mg0. 2O3- δ electrolytes and impregnated nano anodes, ACS Appl. Mater. Interfaces 9 (8) (2017) 7115–7124.
[11] T. Liu, J. Lin, H. Wu, C. Xia, C. Chen, Z. Zhan, Tailoring the pore structure of cathode supports for improving the electrochemical performance of solid oxide fuel cells, J. Electroceram. 40 (2) (2018) 138–143.
[12] M. Liu, Y. Liu, Multilayer tape casting of large-scale anode-supported thin-film electrolyte solid oxide fuel cells, Int. J. Hydrogen Energy 44 (31) (2019) 16976–16982.

[13] D.-S. Tsai, Pressure buildup and internal stresses during binder burnout: numerical analysis, AIChE J. 37 (4) (1991) 547–554.
[14] Z. Fu, A. Roosen, Shrinkage of tape cast products during binder burnout, J. Am. Ceram. Soc. 98 (1) (2015) 20–29.
[15] W.J. Tseng, C.-K. Hsu, Cracking defect and porosity evolution during thermal debinding in ceramic injection moldings, Ceram. Int. 25 (5) (1999) 461–466.
[16] S. Virdhian, T. Osada, H.G. Kang, F. Tsumori, H. Miura, Evaluation and analysis of distortion of complex shaped Ti-6Al-4V compacts by metal injection molding process, in: Key Engineering Materials, Vol. 520, Trans Tech Publ, 2012, pp. 187–194.
[17] P. Wongpanit, S. Khanthsri, S. Puengboonsri, A. Manonukul, Effects of acrylic acid-grafted HDPE in HDPE-based binder on properties after injection and debinding in metal injection molding, Mater. Chem. Phys. 147 (1–2) (2014) 238–246.
[18] Y. Shengjie, Y. Lam, S. Yu, K. Tam, Thermal debinding modeling of mass transport and deformation in powder-injection molding compact, Metall. Mater. Trans. B 33 (3) (2002) 477–488.
[19] M. Belgacem, B. Thierry, G. Jean-Claude, Investigations on thermal debinding process for fine 316L stainless steel feedstocks and identification of kinetic parameters from coupling experiments and finite element simulations, Powder Technol. 235 (2013) 192–202.
[20] M. Barone, J. Ulicny, Liquid-phase transport during removal of organic binders in injection-molded ceramics, J. Am. Ceram. Soc. 73 (11) (1990) 3323–3333.
[21] L. Khoong, Y. Lam, J. Chai, L. Jiang, J. Ma, Numerical and experimental investigations on thermal debinding of polymeric binder of powder injection molding compact, Chem. Eng. Sci. 62 (23) (2007) 6927–6938.
[22] K. Feng, S.J. Lombardo, Modeling of the pressure distribution in three-dimensional porous green bodies during binder removal, J. Am. Ceram. Soc. 86 (2) (2003) 234–240.
[23] A.C. West, S.J. Lombardo, The role of thermal and transport properties on the binder burnout of injection-molded ceramic components, Chem. Eng. J. 71 (3) (1998) 243–252.
[24] Y. Bae, S. Lee, K.J. Yoon, J.-H. Lee, J. Hong, Three-dimensional dynamic modeling and transport analysis of solid oxide fuel cells under electrical load change, Energy Convers. Manage. 165 (2018) 405–418.
[25] M. Navasa, X.-Y. Miao, H.L. Frandsen, A fully-homogenized multiphysics model for a reversible solid oxide cell stack, Int. J. Hydrogen Energy 44 (41) (2019) 23330–23347.
[26] X.-Y. Miao, O.B. Rizvandi, M. Navasa, H.L. Frandsen, Modelling of local mechanical failures in solid oxide cell stacks, Appl. Energy 293 (2021) 116901.
[27] X. Zhuang, Q. Wang, H. Zhu, A 3D computational homogenization model for porous material and parameters identification, Comput. Mater. Sci. 96 (2015) 536–548.
[28] G. Reiss, H.L. Frandsen, W. Brandstätter, A. Weber, Numerical evaluation of micro-structural parameters of porous supports in metal-supported solid oxide fuel cells, J. Power Sources 273 (2015) 1006–1015.
[29] G. Reiss, H.L. Frandsen, Å.H. Persson, C. Weiß, W. Brandstätter, Numerical evaluation of oxide growth in metallic support microstructures of solid oxide fuel cells and its influence on mass transport, J. Power Sources 297 (2015) 388–399.
[30] B. Nait-Ali, K. Haberko, H. Vesteghem, J. Absi, D. Smith, Thermal conductivity of highly porous zirconia, J. Eur. Ceram. Soc. 26 (16) (2006) 3567–3574.
[31] VDM-Metals, Crofer 22 APU, Brochure, 2021, URL https://www.vdm-metals.com/fileadmin/user_upload/Downloads/Data_Sheets/Data_Sheet_VDM_Crofer_22_APU.pdf.
[32] K. Dubyk, M. Isaiev, S. Alekseev, R. Burbelo, V. Lysenko, Thermal conductivity of nanofluids formed by carbon flurooxide mesoparticles, SN Appl. Sci. 1 (11) (2019) 1–7.
[33] MIT, PMMA, 2018, https://www.mit.edu/~6.777/matprops/pmma.htm, Accessed: 03-03-2022.
[34] X. Lu, B. Liang, X. Sheng, T. Yuan, J. Qu, Enhanced thermal conductivity of polyurethane/wood powder composite phase change materials via incorporating low loading of graphene oxide nanosheets for solar thermal energy storage, Sol. Energy Mater. Sol. Cells 208 (2020) 110391.
[35] G. Wypych, Handbook of Fillers, Vol. 938, ChemTec Publishing Toronto, 2016.
[36] H.E. Kissinger, Reaction kinetics in differential thermal analysis, Anal. Chem. 29 (11) (1957) 1702–1706.
[37] J. Criado, L. Pérez-Maqueda, P. Sánchez-Jiménez, Dependence of the pre-exponential factor on temperature, J. Therm. Anal. Calorim. 82 (3) (2005) 671–675.
[38] J. Kozeny, Uber kapillare leitung der wasser in boden, R. Acad. Sci. Vienna, Proc. Class I 136 (1927) 271–306.
[39] P.C. Carman, Fluid flow through granular beds, Trans. Am. Inst. Chem. Eng. 15 (1937) 150–166.
[40] C.F. Berg, Permeability description by characteristic length, tortuosity, constriction and porosity, Transp. Porous Media 103 (3) (2014) 381–400.